

Supplementary Material for:

Reduced anharmonic phonon scattering cross-section slows the decrease of thermal conductivity with temperature

Xiaolong Yang^{1*}, Janak Tiwari², and Tianli Feng^{2†}

¹College of Physics and Center of Quantum Materials and Devices, Chongqing University, Chongqing 401331, China.

²Department of Mechanical Engineering, University of Utah, Salt Lake City, Utah 84112, USA.

Corresponding Authors:

*Email: yangxl@cqu.edu.cn

†Email: tianli.feng@utah.edu

A. Three- and four-phonon scattering rates calculations

The three- and four-phonon scattering rates, $\tau_{3,\lambda}^{-1}$ and $\tau_{4,\lambda}^{-1}$, are calculated by Fermi's golden rule (FGR)¹:

$$\tau_{3,\lambda}^{-1} = \sum_{\lambda'\lambda''} \left[\frac{1}{2} (1 + n_{\lambda'}^0 + n_{\lambda''}^0) \mathcal{L}_- + (n_{\lambda'}^0 - n_{\lambda''}^0) \mathcal{L}_+ \right], \quad (\text{S.1})$$

$$\tau_{4,\lambda}^{-1} = \sum_{\lambda'\lambda''\lambda'''} \left[\frac{1}{6} \frac{n_{\lambda'}^0 n_{\lambda''}^0 n_{\lambda'''}^0}{n_{\lambda}^0} \mathcal{L}_{--} + \frac{1}{2} \frac{(1 + n_{\lambda'}^0) n_{\lambda''}^0 n_{\lambda'''}^0}{n_{\lambda}^0} \mathcal{L}_{+-} + \frac{1}{2} \frac{(1 + n_{\lambda'}^0)(1 + n_{\lambda''}^0) n_{\lambda'''}^0}{n_{\lambda}^0} \mathcal{L}_{++} \right]. \quad (\text{S.2})$$

Here λ stands for (\mathbf{q}, j) with \mathbf{q} and j labeling the phonon wave vector and dispersion branch, respectively.

$n^0 = \left(e^{\frac{\hbar\omega}{k_B T}} - 1 \right)^{-1}$ is the phonon occupation number, and ω is the phonon angular frequency. The

transition probability matrix \mathcal{L} is determined by the third-order and fourth-order interatomic force constants (IFCs) ¹:

$$\mathcal{L}_{\pm} = \frac{\pi\hbar}{4N_{\mathbf{q}}} \left| V_{\pm}^{(3)} \right|^2 \Delta_{\pm} \frac{\delta(\omega_{\lambda} \pm \omega_{\lambda'} - \omega_{\lambda''})}{\omega_{\lambda} \omega_{\lambda'} \omega_{\lambda''}}, \quad (\text{S.3})$$

$$\mathcal{L}_{\pm\pm} = \frac{\pi\hbar}{4N_{\mathbf{q}}} \frac{\hbar}{2N_{\mathbf{q}}} \left| V_{\pm\pm}^{(4)} \right|^2 \Delta_{\pm\pm} \frac{\delta(\omega_{\lambda} \pm \omega_{\lambda'} \pm \omega_{\lambda''} - \omega_{\lambda'''})}{\omega_{\lambda} \omega_{\lambda'} \omega_{\lambda''} \omega_{\lambda'''}}}, \quad (\text{S.4})$$

where $V_{\pm}^{(3)}$ and $V_{\pm\pm}^{(4)}$ are

$$V_{\pm}^{(3)} = \sum_{b,l_1 b_1, l_2 b_2} \sum_{\alpha \alpha_1 \alpha_2} \phi_{0b, l_1 b_1, l_2 b_2}^{\alpha \alpha_1 \alpha_2} \frac{e_{ab}^{\lambda} e_{\alpha_1 b_1}^{\pm \lambda'} e_{\alpha_2 b_2}^{-\lambda''}}{\sqrt{\bar{m}_b \bar{m}_{b_1} \bar{m}_{b_2}}} e^{(\pm i \mathbf{q}' \cdot \mathbf{r}_{l_1} - i \mathbf{q}'' \cdot \mathbf{r}_{l_2})}, \quad (\text{S.5})$$

$$V_{\pm\pm}^{(4)} = \sum_{b, l_1 b_1, l_2 b_2, l_3 b_3} \sum_{\alpha \alpha_1 \alpha_2 \alpha_3} \phi_{0b, l_1 b_1, l_2 b_2, l_3 b_3}^{\alpha \alpha_1 \alpha_2 \alpha_3} \frac{e_{ab}^{\lambda} e_{\alpha_1 b_1}^{\pm \lambda'} e_{\alpha_2 b_2}^{\pm \lambda''} e_{\alpha_3 b_3}^{-\lambda'''}}{\sqrt{\bar{m}_b \bar{m}_{b_1} \bar{m}_{b_2} \bar{m}_{b_3}}} e^{(\pm i \mathbf{q}' \cdot \mathbf{r}_{l_1} \pm i \mathbf{q}'' \cdot \mathbf{r}_{l_2} - i \mathbf{q}''' \cdot \mathbf{r}_{l_3})}, \quad (\text{S.6})$$

$N_{\mathbf{q}}$ is the total number of \mathbf{q} points. The Kronecker deltas $\Delta_{\pm} = \Delta_{\mathbf{q} \pm \mathbf{q}' - \mathbf{q}'', \mathbf{R}}$ and $\Delta_{\pm\pm} = \Delta_{\mathbf{q} \pm \mathbf{q}' \pm \mathbf{q}'' - \mathbf{q}''', \mathbf{R}}$ describe the momentum selection rule and have the property that $\Delta_{m,n} = 1$ (if $m = n$), or 0 (if $m \neq n$). \mathbf{R} is a reciprocal lattice vector. $\phi_{0b, l_1 b_1, l_2 b_2}^{\alpha \alpha_1 \alpha_2}$ and $\phi_{0b, l_1 b_1, l_2 b_2, l_3 b_3}^{\alpha \alpha_1 \alpha_2 \alpha_3}$ are the third- and fourth-order force constants, which are calculated from DFT. l, b , and α label the indices of unit cells, basis atoms, and Cartesian directions, respectively. \mathbf{r}_l is the position of the unit cell l . \bar{m}_b is the average atomic mass at the lattice site b . e is the phonon eigenvector component. The eigenvectors are solved by using the dynamical matrix shown in Phonopy². Details of correctly using the eigenvectors together with the phase term $\exp(i \mathbf{q} \cdot \mathbf{r})$ can be found in Ref.³.

B. Lattice thermal conductivity calculations

The thermal conductivity along a crystal orientation κ_α ($\alpha = x, y, z$) is calculated by using the exact solution to the Boltzmann transport equation^{4,5},

$$\kappa_\alpha = \frac{1}{V} \sum_{\lambda} v_{\alpha,\lambda}^2 c_\lambda \tau_\lambda^{it}, \quad (\text{S.7})$$

where V is crystal volume, v_α is phonon group velocity projection along the direction α , and c_λ is phonon specific heat per mode. τ_λ^{it} is the phonon relaxation time solved by an iterative scheme:

$$\tau_\lambda^{it} = \tau_\lambda (1 + \Theta_\lambda), \quad (\text{S.8})$$

$$\frac{1}{\tau_\lambda} = \tau_{3,\lambda}^{-1} + \tau_{4,\lambda}^{-1} + \sum_{\lambda' \neq \lambda} \Gamma_{\lambda\lambda'}^{\text{iso}}, \quad (\text{S.9})$$

$$\Gamma_{\lambda\lambda'}^{\text{iso}} = \frac{\pi}{2N_c} \omega_\lambda \omega_{\lambda'} \sum_b^n g_b |\mathbf{e}_\lambda^b \cdot \mathbf{e}_{\lambda'}^{b*}|^2 \delta(\omega_\lambda - \omega_{\lambda'}), \quad (\text{S.10})$$

$$g_b = \sum_i f_{ib} \left(1 - \frac{m_{ib}}{\bar{m}_b}\right)^2, \quad (\text{S.11})$$

$$\Theta_\lambda = \sum_{\lambda'\lambda''}^{(+)} \mathcal{L}_+ (\xi_{\lambda\lambda''} \tau_{\lambda''}^{it} - \xi_{\lambda\lambda'} \tau_{\lambda'}^{it}) + \sum_{\lambda'\lambda''}^{(-)} \frac{1}{2} \mathcal{L}_- (\xi_{\lambda\lambda''} \tau_{\lambda''}^{it} + \xi_{\lambda\lambda'} \tau_{\lambda'}^{it}) + \sum_{\lambda' \neq \lambda} \Gamma_{\lambda\lambda'}^{\text{iso}} \xi_{\lambda\lambda'} \tau_{\lambda'}^{it}, \quad (\text{S.12})$$

where $\xi_{\lambda\lambda'} = v_{\lambda',\alpha} \omega_{\lambda'} / v_{\lambda,\alpha} \omega_\lambda$. Equation (S.8) is solved iteratively because both the left and the right-hand sides contain the unknown variable τ_λ^{it} , and thus the method is called Iterative Scheme. g_b characterizes the magnitude of mass disorder induced by isotopes in lattice, where i indicates isotope types, f_{ib} is the fraction of isotope i in lattice sites of basis atom b , m_{ib} is the mass of isotope i , \bar{m}_b is the average atom mass of basis b sites. \mathbf{e} is the phonon eigenvectors.

The thermal conductivities w/o four-phonon scattering is determined by including the $\tau_{4,\lambda}^{-1}$ term in Eq. (S.9) or not. The evaluations of Eqs. (S7) – (S12) are done by using ShengBTE package⁶ with the FourPhonon extension module⁷.

C. Impact of grain size and vacancy defects

The scattering rate of the grain boundary defects is calculated using equation S.13. Here, λ is short for a phonon mode (\mathbf{q}, j) with \mathbf{q} and j labeling the phonon wave vector and dispersion branch, respectively. $\tau_{gb,\lambda}$ represents the relaxation time of phonon at λ , v_{ph} represents the phonon group velocity, and D_{grain} is the grain size. The method used in the calculation is similar as described in Ref.⁸

$$\tau_{gb,\lambda}^{-1} = \frac{v_{ph,\lambda}}{D_{grain}} \quad (\text{S.13})$$

$$\tau_{d,\lambda}^{-1} = 9 \frac{\pi}{2} * f_v * \left(1 - \frac{m_v}{\bar{m}_b}\right)^2 * \omega_\lambda^2 * pDOS(\omega) \quad (\text{S.14})$$

The scattering rate of the crystal with vacancy defects is estimated using equation S.14. In the equation, f_v represents the concentration of the vacancy (either oxygen vacancy or uranium vacancy); m_v represents the mass of the vacancy (which is equal to zero); and \bar{m}_b represents the mass of the basis atom. Similarly, ω represents the angular velocities and $pDOS(\omega)$ represents the partial density of states of a basis atom. For example, to calculate the scattering rate of oxygen vacancy, f_v is oxygen vacancy, \bar{m}_b is the atomic mass of oxygen, and $pDOS(\omega)$ is the partial density of states of oxygen atoms.

The coefficient 9 in equation S.13 accounts for the mass and bond loss associated with the defect vacancy^{9,10}. The $pDOS(\omega)$ of the atoms is calculated so that the weighted sum of $pDOS$ of all the atoms equals unity. The lattice thermal conductivity of the crystal with vacancy defect is then estimated based on the calculated scattering rate. The phonon dispersion and IFCs are the same as those of perfect crystals.

D. Interatomic force constants (IFCs) calculation

The ground-state 2nd, 3rd, and 4th-order IFCs are calculated by a finite displacement method using *Phonopy*², *Thirdorder*⁶, and *Fourthorder*⁷, respectively. The interatomic forces with specific atomic displacements needed for these calculations are obtained by using the Vienna ab initio simulation package (VASP)^{11–13}.

The temperature-dependent IFCs are obtained from the temperature-dependent effective potential (TDEP) method^{14–16}. The TDEP method extracts effective IFCs at a certain temperature by fitting the potential energy of a series of atomic trajectory images from ab initio molecular dynamics (AIMD) simulations at that temperature to the 2nd, 3rd, and 4th orders. To greatly reduce the computational cost, here the AIMD simulations for the TDEP calculation are replaced by the classical molecular dynamics based on machine-learning potential. Given the high efficiency and accuracy of moment tensor potential (MTP)^{17–19} as demonstrated by previous studies^{20,21}, we choose the MTP to develop an interatomic potential of UO₂ by learning from the AIMD based data. The framework of MTP and the details of potential parameterization is presented in Section E.

E. Moment tensor potentials

MTP is a local potential with a form with a linear combination of polynomial basis functions representing one-body, two-body, and many-body interactions^{17–19}. In the framework of the MTP, the total energy E of an atomic configuration with N atoms is the summation of contributions V of neighborhoods u_i of each i -th atom: $E^{\text{MTP}} = \sum_{i=1}^N V(u_i)$. The interatomic potential V can be expressed as a linear combination of a set of basis functions $\mathbf{B}_k(u_i)$:

$$V(u_i) = \sum_k \boldsymbol{\theta}_k \mathbf{B}_k(u_i),$$

where θ_k are the MTP parameters determined by minimizing the energy, forces, and virial stresses differences between E_{mtp} and AIMD results on a training set of configurations. $\mathbf{B}_k(u_i)$ are constructed with all possible contractions of the moment tensor descriptors $\mathbf{M}_{\mu\nu}(i)$ including the radial f_μ and angular part $\mathbf{r}_{ij}^{\oplus\nu}$, given as

$$\mathbf{M}_{\mu\nu}(i) = \sum_j f_\mu(|r_{ij}|, S_i, S_j) \mathbf{r}_{ij}^{\oplus\nu},$$

where r_{ij} is the distance of atom j relative to atom i , S is the type of atoms, and $\mathbf{r}_{ij}^{\oplus\nu}$ is the Kronecker product of ν copies of \mathbf{r}_{ij} . Full expressions for $f_\mu(|r_{ij}|, S_i, S_j)$ can be found in Ref. ¹⁷⁻¹⁹. The MTP parameters are obtained by minimizing the error between the AIMD results and the MTP results:

$$\min_{\mathbf{K}} \sum \{w_e \Delta E + w_f \Delta f + w_s \Delta \sigma\},$$

where ΔE , Δf , and $\Delta \sigma$ are the energy, force, and stress error between the AIMD data and the MTP results. w_e , w_f , w_s are weight factors of energy, forces, and stresses, respectively. \mathbf{K} is the training set with different atomic configurations.

In the present work, we use the functional form of MTP of level 26 and 6 radial basis functions so as to achieve a trade-off between the computational cost and the accuracy of MTP. The cutoff distance is set to 5 Å, which enables the convergence of thermal conductivity with anharmonicity up to the third order. During the optimization, the fitting weights are set to default values, namely $w_e = 1$, $w_f = 0.1$, and $w_s = 0.001$, which have been proven to be accurate in previous works^{19,21-23}.

F. Computational details

All density functional theory (DFT) calculations were carried out using the Vienna *Ab initio* Simulation Package (VASP)¹¹ with the projector augmented wave method (PAW) and the plane-wave energy cutoff of 500 eV. The generalized gradient approximation (GGA) of Perdew-Burke-Ernzerhof (PBE)²⁴

exchange-correlation functional was used for UO_2 , and the local density approximation (LDA)²⁴ exchange-correlation functional was used for Si and Ge. The lattices and internal atomic positions were fully relaxed with the total energy convergence threshold of 1×10^{-10} eV and a criterion of 1×10^{-4} eV \AA^{-1} for the forces on each atom, respectively. Note that the standard DFT calculations fail to simulate the strong correlations among the U $5f$ electrons as mentioned previously^{25–28}, and the use of more powerful theoretical approaches such as hybrid functional density functional theory²⁹ and dynamical mean field theory³⁰ represents an important direction for future simulations. However, the significantly higher computational requirements for such approaches have so far precluded their ability to predict the electronic and phonon behaviors. Here, we adopted GGA with Hubbard-U correction (GGA+U)³¹ using the effective Hubbard parameter $U=4.5$ eV and $J=0.51$ eV^{25,26,32,33} to deal with the physical properties of UO_2 . Despite that this method does not fully include the $5f$ strong correlation effects and may fail in calculating some properties, it is still of high fidelity in producing interatomic force constant and thus phonon dispersion curves. In addition to the fact that GGA+U is necessary to reproduce good electronic band gap^{31,34–36}, we find that it is necessary to produce a better dispersion compared to GGA.

To generate the training sets for the MTPs, we performed AIMD simulations for 1 *ps* under the isobaric-isothermal (NPT) ensemble with a time step of 1 *fs* for $2 \times 2 \times 2$ UO_2 conventional cells at finite temperatures from 100 to 2200 K with the interval of 100 K, and for $4 \times 4 \times 4$ Si and Ge primitive cells at temperatures ranging from 100 to 1000 K with the mesh of 100 K. The Monkhorst–Pack grid of $2 \times 2 \times 2$ was used in the AIMD simulations. The forces, energies, and stresses extracted from 965, 814, and 740 uncorrelated configurations for UO_2 , Si, and Ge were selected by the MLIP package¹⁸ to train the MTP, respectively.

In the ground-state IFCs calculations, $5 \times 5 \times 5$ primitive cells were used with the Monkhorst–Pack grid of $3 \times 3 \times 3$. We used the interatomic forces of configurations extracted from the trained MTP as inputs of *Phonopy*², *Thirdorder*⁶, and *Fourthorder*⁷ to calculate the 2nd, 3rd, and 4th -order IFCs, respectively. The 3rd and 4th-order IFCs were calculated including up to fifth and second nearest neighbors, respectively, which has been proven to be enough for the convergence of κ ^{7,23,37}.

To calculate the temperature-dependent IFCs, the TDEP package^{14–16} was employed using the potential energy of a series of atomic trajectory images as inputs. To generate the potential energy of a series of atomic trajectories, we used the trained MTP to conduct the classical MD simulations for $5 \times 5 \times 5$ UO_2

primitive cells at finite temperatures from 100 to 2200 K with the interval of 100 K, as implemented in the parallel molecular dynamics package LAMMPS³⁸ and MTP. At each temperature, the system was first relaxed in the NPT ensemble using the Nose-Hoover thermostat for 50 *ps*. Then the system was run for further 100 *ps* to sample the forces, energies, and stresses data for each configuration with the time interval of 0.1 *ps*. Using these samples as inputs of the TDEP package, the 2nd, 3rd, and 4th -order IFCs were computed.

With these IFCs, the lattice thermal conductivity was computed by solving the Boltzmann transport equation (BTE) with an iterative scheme, as implemented in the ShengBTE^{6,7} package. To effectively reduce the computational cost, herein the isotopic scattering and three-phonon scattering were included to solve the BTE iteratively while four-phonon scattering was considered at the level of the relaxation time approximation, which has been demonstrated to be valid in various materials^{1,7,37,39}. Besides, the boundary scattering was considered by the simple empirical form: $\frac{1}{\tau_b} = |v_\lambda|/L$ when the size (*L*) effect is involved. Finally, the thermal conductivity was solved with a $12 \times 12 \times 12$ **q**-mesh, which enables a good convergence of κ , as shown in Fig.S10 in the Supplemental Material.

G. Impact of oxygen and uranium vacancies on thermal transport

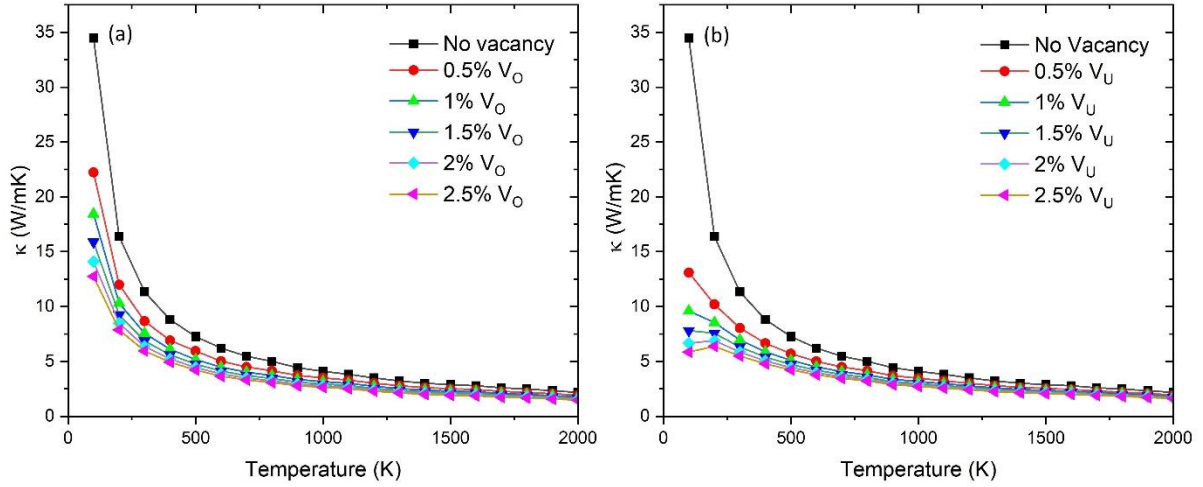


Figure S1. Impacts of oxygen and uranium vacancy defects on the lattice κ of the UO_2 (a) oxygen vacancy (V_O) and (b) uranium vacancy (V_U). The lattice κ decreases with oxygen and uranium vacancy defects. For the maximum V_O studied (2.5%), κ reduces by 63% and 32.37% for the temperature of 100K and 2000K, respectively. Similarly, for 2.5% V_U defect, lattice κ reduces by 83% and 25.54% for the temperature of 100K and 2000K, respectively. The black line (No vacancy) represents the pure crystal without any oxygen or uranium vacancy defects.

H. Three and four-phonon scattering rates in UO_2

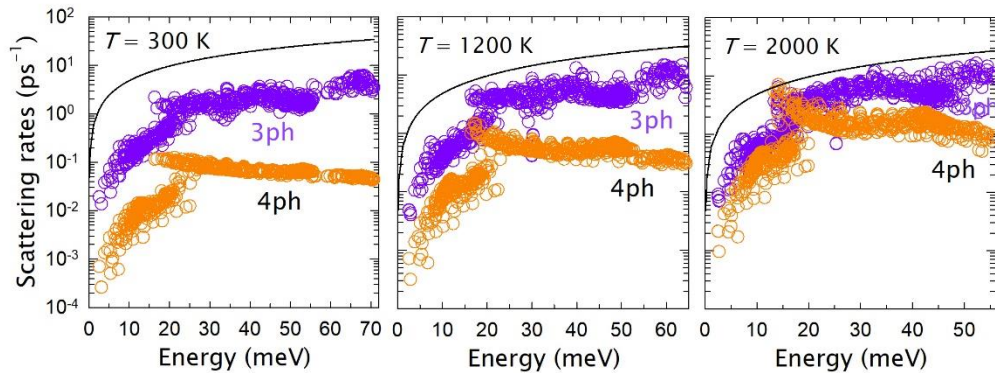


Figure S2. Phonon scattering rates of UO_2 at 300 K, 1200 K, and 2000 K, calculated using temperature-dependent IFCs.

I. Si and Ge thermal conductivity

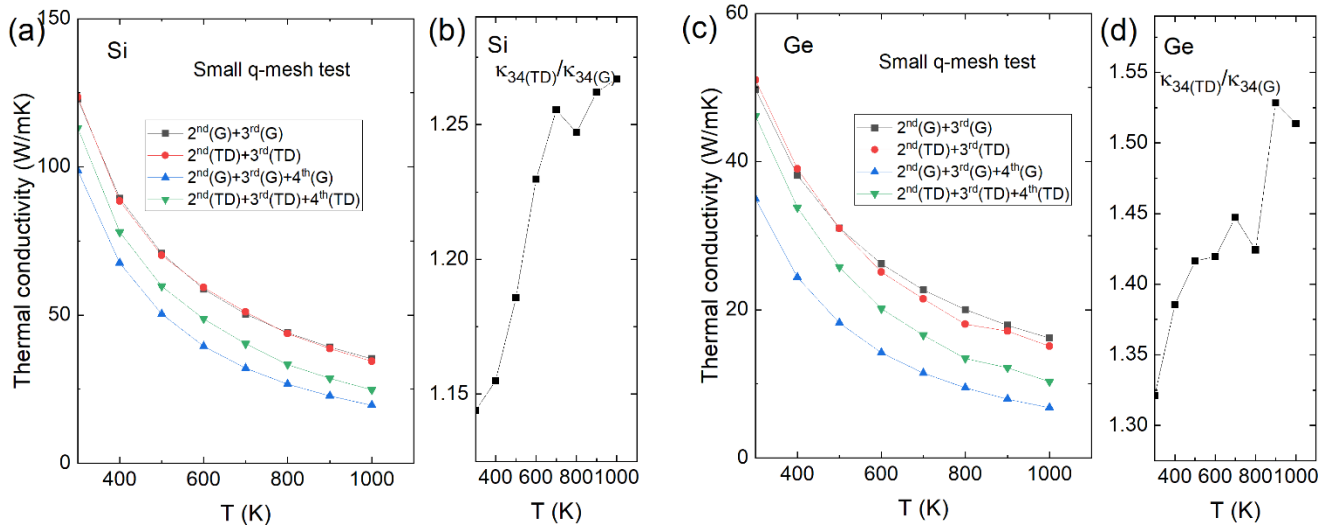


Figure S3. Small q-mesh ($12 \times 12 \times 12$) tests on the thermal conductivities of Si and Ge using various IFCs. Here we do not compare the results with experiment because a $36 \times 36 \times 36$ q-mesh is necessary to get a converged thermal conductivity. Also, exchange-correlation function selection can have an impact on the final results. Here, we focus on self-consistent comparisons.

J. Phonon dispersion of UO_2

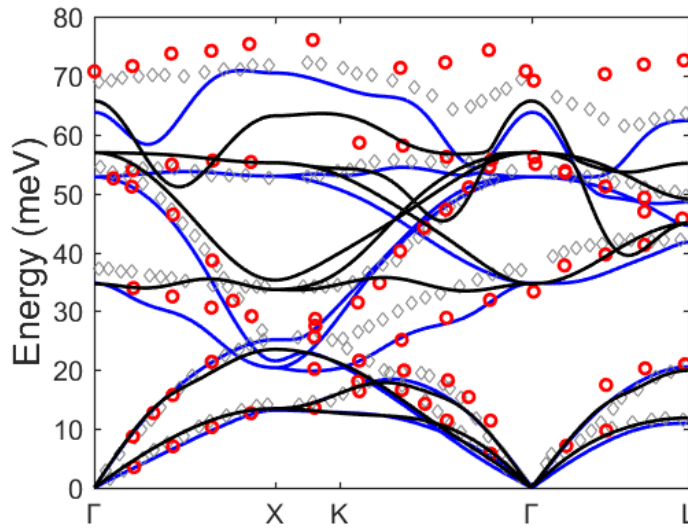


Figure S4. Phonon dispersion relation of UO_2 . Black curve is calculated by ground-state DFT without hubbard U. The blue curve is calculated using GGA+U with machine learning potential fitted from ab initio molecular dynamics at 300 K.

Temperature affects phonon dispersion, as commonly seen in solids, but the impact does not affect much phonon-phonon scattering space that was found in many materials⁴⁰⁻⁴⁴. Therefore, the thermal conductivity increases after considering TD IFCs is not because of phonon dispersion change. The calculated phonon dispersion spectrum along high-symmetry directions together with inelastic neutron scattering data from Refs.^{45,46} are shown in Fig. S4. The overall agreement of the calculated phonon dispersion is very good for the acoustic phonons and fairly good for the optical modes except for the highest one. This situation is similar to all earlier calculations^{45,47-50} using LDA, LDA+U, GGA, GGA+U, and even DMFT, which indicates that it is not an accuracy issue of our machine learning process. It might be because of the many-body interaction for 5f electrons in uranium^{45,51}. Some works attribute such difference to the presence of a certain pressure in experimental measurement⁵⁰. By imposing a pressure, the agreement of this branch agrees better with experiment⁵⁰. The temperature effect on phonon frequency shift as well as broadening is shown in Fig.S5 (b-f).

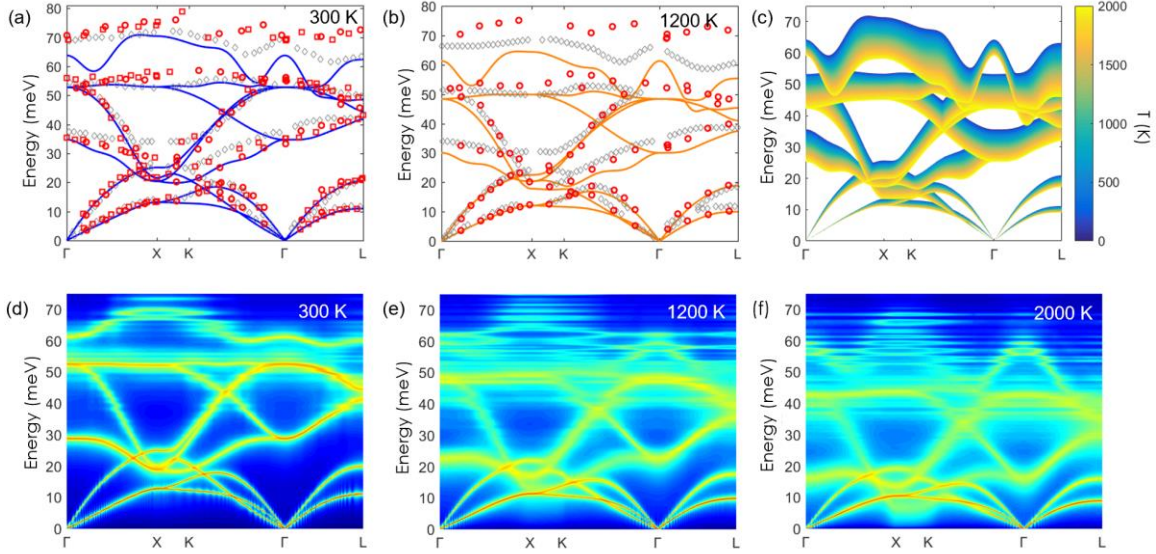


Figure S5. Calculated phonon dispersion of UO_2 at various temperatures. The solid curves in all sub-figures are calculated by using temperature-dependent IFCs in this work. In (a) and (b), the open red and white circles are INS experimental data and DFT calculated data from Ref.⁴⁵, respectively. In (a), the open squares are experimental data from Ref.⁴⁶. In (d-f), the linewidths of curves represent the summation of three and four-phonon scattering rates.

K. The κ convergence test for UO_2

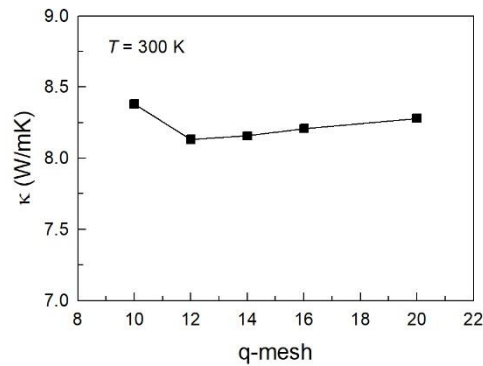


Figure S6. The thermal conductivity without including four-phonon scattering at 300 K of UO_2 with respect to the \mathbf{q} mesh.

1. Feng, T. & Ruan, X. Quantum mechanical prediction of four-phonon scattering rates and reduced thermal conductivity of solids. *Physical Review B* **93**, 045202 (2016).
2. Togo, A. & Tanaka, I. First principles phonon calculations in materials science. *Scripta Materialia* **108**, 1–5 (2015).

3. Feng, T., Yang, X. & Ruan, X. Phonon anharmonic frequency shift induced by four-phonon scattering calculated from first principles. *Journal of Applied Physics* **124**, 145101 (2018).
4. Lindsay, L., Broido, D. a. & Mingo, N. Flexural phonons and thermal transport in graphene. *Physical Review B* **82**, 115427 (2010).
5. Feng, T. & Ruan, X. Four-phonon scattering reduces intrinsic thermal conductivity of graphene and the contributions from flexural phonons. *Physical Review B* **97**, 045202 (2018).
6. Li, W., Carrete, J., Katcho, N. a. & Mingo, N. ShengBTE: A solver of the Boltzmann transport equation for phonons. *Computer Physics Communications* **185**, 1747–1758 (2014).
7. Han, Z., Yang, X., Li, W., Feng, T. & Ruan, X. FourPhonon: An extension module to ShengBTE for computing four-phonon scattering rates and thermal conductivity. *Computer Physics Communications* **270**, 108179 (2022).
8. Xu, B., Feng, T., Li, Z., Pantelides, S. T. & Wu, Y. Constructing Highly Porous Thermoelectric Monoliths with High-Performance and Improved Portability from Solution-Synthesized Shape-Controlled Nanocrystals. *Nano Letters* **18**, 4034–4039 (2018).
9. Ratsifaritana, C. a. & Klemens, P. G. Scattering of phonons by vacancies. *International Journal of Thermophysics* **8**, 737–750 (1987).
10. Xie, G. *et al.* A Bond-order Theory on the Phonon Scattering by Vacancies in Two-dimensional Materials. *Scientific reports* **4**, 5085 (2014).
11. Kresse, G. & Hafner, J. Ab initio molecular dynamics for liquid metlas. *Physical Review B* **47**, 558–561 (1993).
12. Kresse, G. & Hafner, J. Ab initio molecular-dynamics simulation of the liquid-metal–amorphous-semiconductor transition in germanium. *Physical Review B* **49**, 14251–14269 (1994).
13. Kresse, G. & Furthmüller, J. Efficient iterative schemes for ab initio total-energy calculations using a plane-wave basis set. *Phys. Rev. B* **54**, 11169–11186 (1996).
14. Hellman, O. & Abrikosov, I. a. Temperature-dependent effective third-order interatomic force constants from first principles. *Physical Review B* **88**, 144301 (2013).
15. Hellman, O., Abrikosov, I. A. & Simak, S. I. Lattice dynamics of anharmonic solids from first principles. *Physical Review B* **84**, 180301 (2011).
16. Hellman, O., Steneteg, P., Abrikosov, I. a. & Simak, S. I. Temperature dependent effective potential method for accurate free energy calculations of solids. *Physical Review B* **87**, 104111 (2013).
17. Shapeev, A. v. Moment tensor potentials: A class of systematically improvable interatomic potentials. *Multiscale Modeling and Simulation* **14**, 1153–1173 (2016).
18. Novikov, I. S., Gubaev, K., Podryabinkin, E. v & Shapeev, A. v. The MLIP package: moment tensor potentials with MPI and active learning. *Machine Learning: Science and Technology* **2**, 025002 (2021).

19. Mortazavi, B. *et al.* Accelerating first-principles estimation of thermal conductivity by machine-learning interatomic potentials: A MTP/ShengBTE solution. *Computer Physics Communications* **258**, 107583 (2021).
20. Novoselov, I. I., Yanilkin, A. v., Shapeev, A. v. & Podryabinkin, E. v. Moment tensor potentials as a promising tool to study diffusion processes. *Computational Materials Science* **164**, 46–56 (2019).
21. Liu, H., Qian, X., Bao, H., Zhao, C. Y. & Gu, X. High-temperature phonon transport properties of SnSe from machine-learning interatomic potential. *Journal of Physics: Condensed Matter* **33**, 405401 (2021).
22. Mortazavi, B. *et al.* Exploring phononic properties of two-dimensional materials using machine learning interatomic potentials. *Applied Materials Today* **20**, 100685 (2020).
23. Liu, Z., Yang, X., Zhang, B. & Li, W. High Thermal Conductivity of Wurtzite Boron Arsenide Predicted by Including Four-Phonon Scattering with Machine Learning Potential. *ACS Applied Materials & Interfaces* **13**, 53409–53415 (2021).
24. Perdew, J. P., Burke, K. & Ernzerhof, M. Generalized Gradient Approximation Made Simple. *Phys. Rev. Lett.* **77**, 3865–3868 (1996).
25. Dorado, B., Jomard, G., Freyss, M. & Bertolus, M. Stability of oxygen point defects in UO₂ by first-principles DFT+U calculations: Occupation matrix control and Jahn-Teller distortion. *Physical Review B* **82**, 035114 (2010).
26. Chen, Y., Geng, H. Y., Kaneta, Y., Kinoshita, M. & Iwata, S. First principles modeling of stability mechanism of nonstoichiometric uranium dioxide. *Computational Materials Science* **49**, S364–S368 (2010).
27. Yun, Y., Legut, D. & Oppeneer, P. M. Phonon spectrum, thermal expansion and heat capacity of UO₂ from first-principles. *Journal of Nuclear Materials* **426**, 109–114 (2012).
28. Dorado, B. *et al.* First-principles calculations of uranium diffusion in uranium dioxide. *Physical Review B* **86**, 035110 (2012).
29. Becke, A. D. A new mixing of Hartree-Fock and local density-functional theories. *The Journal of Chemical Physics* **98**, 1372–1377 (1993).
30. Kotliar, G. *et al.* Electronic structure calculations with dynamical mean-field theory. *Reviews of Modern Physics* **78**, 865–951 (2006).
31. Dudarev, S. L., Manh, D. N. & Sutton, A. P. Effect of Mott-Hubbard correlations on the electronic structure and structural stability of uranium dioxide. *Philosophical Magazine B: Physics of Condensed Matter; Statistical Mechanics, Electronic, Optical and Magnetic Properties* **75**, 613–628 (1997).
32. Dudarev, S. & Botton, G. Electron-energy-loss spectra and the structural stability of nickel oxide: An LSDA+U study. *Physical Review B - Condensed Matter and Materials Physics* **57**, 1505–1509 (1998).
33. Kim, H., Kim, M. & Kaviani, M. Lattice thermal conductivity of UO₂ using ab-initio and classical molecular dynamics. *Journal of Applied Physics* **115**, 123510 (2014).

34. Dudarev, S. L. *et al.* Electronic structure and elastic properties of strongly correlated metal oxides from first principles: LSD A + U, SIC-LSDA and EELS study of UO₂ and NiO. *Physica Status Solidi (A) Applied Research* **166**, 429–443 (1998).
35. Prodan, I. D., Scuseria, G. E. & Martin, R. L. Covalency in the actinide dioxides: Systematic study of the electronic properties using screened hybrid density functional theory. *Physical Review B - Condensed Matter and Materials Physics* **76**, 2–5 (2007).
36. Yun, Y., Kim, H., Lim, H. & Park, K. Electronic structure of UO₂ from the density functional theory with on-site Coulomb repulsion. *Journal of the Korean Physical Society* **50**, 1285–1289 (2007).
37. Feng, T., Lindsay, L. & Ruan, X. Four-phonon scattering significantly reduces intrinsic thermal conductivity of solids. *Physical Review B* **96**, 161201 (2017).
38. Plimpton, S. Fast parallel algorithms for short-range molecular dynamics. *Journal of computational physics* **117**, 1–19 (1995).
39. Yang, X., Feng, T., Li, J. & Ruan, X. Stronger role of four-phonon scattering than three-phonon scattering in thermal conductivity of III-V semiconductors at room temperature. *Physical Review B* **100**, 245203 (2019).
40. Xia, Y. *et al.* High-Throughput Study of Lattice Thermal Conductivity in Binary Rocksalt and Zinc Blende Compounds Including Higher-Order Anharmonicity. *Physical Review X* **10**, 041029 (2020).
41. Xia, Y., Pal, K., He, J., Ozoliņš, V. & Wolverton, C. Particlelike Phonon Propagation Dominates Ultralow Lattice Thermal Conductivity in Crystalline Ti₃VSe₄. *Physical Review Letters* **124**, 065901 (2020).
42. Xia, Y., Ozoliņš, V. & Wolverton, C. Microscopic Mechanisms of Glasslike Lattice Thermal Transport in Cubic Cu₁₂Sb₄S₁₃ Tetrahedrites. *Physical Review Letters* **125**, 43–46 (2020).
43. Xia, Y. Revisiting lattice thermal transport in PbTe: The crucial role of quartic anharmonicity. *Applied Physics Letters* **113**, 073901 (2018).
44. Ravichandran, N. K. & Broido, D. Unified first-principles theory of thermal properties of insulators. *Physical Review B* **98**, 085205 (2018).
45. Pang, J. W. L. *et al.* Phonon Lifetime Investigation of Anharmonicity and Thermal Conductivity of UO₂ by Neutron Scattering and Theory. *Physical Review Letters* **110**, 157401 (2013).
46. Dolling, G., Cowley, R. A. & Woods, A. D. B. The crystal dynamics of uranium dioxide. *Canadian Journal of Physics* **43**, 1397 (1965).
47. Yin, Q. & Savrasov, S. Y. Origin of low thermal conductivity in nuclear fuels. *Physical Review Letters* **100**, 1–4 (2008).
48. Wang, B.-T., Zhang, P., Lizárraga, R., di Marco, I. & Eriksson, O. Phonon spectrum, thermodynamic properties, and pressure-temperature phase diagram of uranium dioxide. *Physical Review B* **88**, 104107 (2013).
49. Sanati, M., Albers, R. C., Lookman, T. & Saxena, A. Elastic constants, phonon density of states, and thermal properties of UO₂. *Physical Review B - Condensed Matter and Materials Physics* **84**, 1–7 (2011).

50. Kaur, G., Panigrahi, P. & Valsakumar, M. C. Thermal properties of UO₂ with a non-local exchange-correlation pressure correction: a systematic first principles DFT + U study. *Modelling and Simulation in Materials Science and Engineering* **21**, 065014–065014 (2013).
51. Gofryk, K. *et al.* Anisotropic thermal conductivity in uranium dioxide. *Nature Communications* **5**, 4551 (2014).